The Yermak Pass Branch: a major pathway for the Atlantic water north of Svalbard?

Zoé Koenig, Christine Provost, Nathalie Sennéchael, Gilles Garric, Jean-Claude Gascard

AGU PUBLICATIONS

JGR

Journal of Geophysical Research: Oceans

RESEARCH ARTICLE

10.1002/2017JC013271

The Yermak Pass Branch: A Major Pathway for the Atlantic Water North of Svalbard?

Zoé Koenig[1], Christine Provost[1], Nathalie Sennéchael[1], Gilles Garric[2], and Jean-Claude Gascard[1]

[1]Laboratoire LOCEAN-IPSL, Sorbonne Universités (UPMC, Univ. Paris 6)-CNRS-IRD-MNHN, Paris, France, [2]Mercator Ocean, Research and Development, Ramonville Saint-Agne, France

Key Points:
- ADCP data gathered in 2007–2008 in the ice-covered Yermak Pass show that tides induce a rectified mean current of a few cm/s
- Atlantic Water eddies with 5–15 day periods and Atlantic Water pulses of 1–2 month duration are observed in the Yermak Pass in winter
- In 1/12° Mercator-Ocean operational model outputs, the Yermak Pass Branch carries about 30% of the volume transport of the WSC

Correspondence to:
Z. Koenig,
zklod@locean-ipsl.upmc.fr

Citation:
Koenig, Z., Provost, C., Sennéchael, N., Garric, G., & Gascard, J.-C. (2017). The Yermak Pass Branch: A major pathway for the Atlantic Water north of Svalbard? *Journal of Geophysical Research: Oceans*, *122*, 9332–9349. https://doi.org/10.1002/2017JC013271

Received 13 JUL 2017
Accepted 5 OCT 2017
Accepted article online 27 OCT 2017
Published online 1 DEC 2017

Abstract An upward-looking Acoustic Doppler Current Profiler deployed from July 2007 to September 2008 in the Yermak Pass, north of Svalbard, gathered velocity data from 570 m up to 90 m at a location covered by sea ice 10 months out of 12. Barotropic diurnal and semidiurnal tides are the dominant signals in the velocity (more than 70% of the velocity variance). In winter, baroclinic eddies at periods between 5 and 15 days and pulses of 1–2 month periodicity are observed in the Atlantic Water layer and are associated with a shoaling of the pycnocline. Mercator-Ocean global operational model with daily and 1/12° spatial resolution is shown to have skills in representing low-frequency velocity variations (>1 month) in the West Spitsbergen Current and in the Yermak Pass. Model outputs suggest that the Yermak Pass Branch has had a robust winter pattern over the last 10 years, carrying on average 31% of the Atlantic Water volume transport of the West Spitsbergen Current (36% in autumn/winter). However, those figures have to be considered with caution as the model neither simulates tides nor fully resolves eddies and ignores residual mean currents that could be significant.

1. Introduction

The Atlantic Water (AW) supplies heat and salt to the Arctic Ocean impacting the thermohaline structure of the water column and influencing the distribution of sea ice (e.g., Rudels, 2012). Despite the importance of AW to the Arctic system, the AW inflow (pathways and volume transports) north of Svalbard is still poorly documented in part because of the large sea-ice cover at all seasons.

In Fram Strait, the Atlantic Water flows along the west coast of Svalbard through the West Spitsbergen Current (WSC; Figure 1a). The WSC has been monitored since 1997 with a mooring array deployed at 78.5°N in collaboration between the Norwegian Polar Institute (NPI, Norway) and the Alfred-Wegener Institute (AWI, Germany). The seasonal variability of the Atlantic Water inflow is important, with a stronger and warmer flow in winter than in summer in the WSC (Beszczynska-Möller et al., 2012). The WSC is unstable (e.g., Teigen et al., 2010, 2011) thereby generating eddies in the Fram Strait. The Yermak Plateau located to the northwest of Svalbard is a main obstacle to the warm AW inflow into the Arctic and the WSC splits into branches as isobaths diverge (Figure 1a). One branch, the shallow Svalbard Branch, follows the 400–500 m isobaths of the continental slope inshore of the Yermak Plateau (Cokelet et al., 2008; Muench et al., 1992; Sirevaag et al., 2011). Other branches recirculate cyclonically following the topographic fracture zones (FZ; Molloy FZ at 79°N and Spitzbergen FZ at 80.5°N) directly through Fram Strait (Teigen et al., 2011). The Fram Strait recirculating branches are largely dominated by eddies (Gascard et al., 1995; Hattermann et al., 2016; Von Appen et al., 2016). Another branch, the deeper Yermak branch flows along the western shelf of the Yermak Plateau above the 1,500 m isobath (Manley, 1995; Manley et al., 1992). Yet another path, the Yermak Pass Branch, was discovered using acoustically tracked neutrally buoyant floats during the ARCTEMIZ88 experiment (Gascard et al., 1995). Five floats, stabilized around 310–350 m, made a spectacular U turn at about 80.8°N following the 700–800 m isobaths and crossed the Yermak Plateau through the Yermak Pass in the fall 1988 (Figure 1b). The lack of year-round observations over the ice-covered Yermak Plateau may explain why the Yermak Pass Branch has not been documented since the unique float drifts of fall 1988.

Twenty-eight months (January 2014 to April 2016) of outputs from Mercator-Ocean global operational system have been used, after a careful evaluation, to examine the circulation of Atlantic Water at the entrance

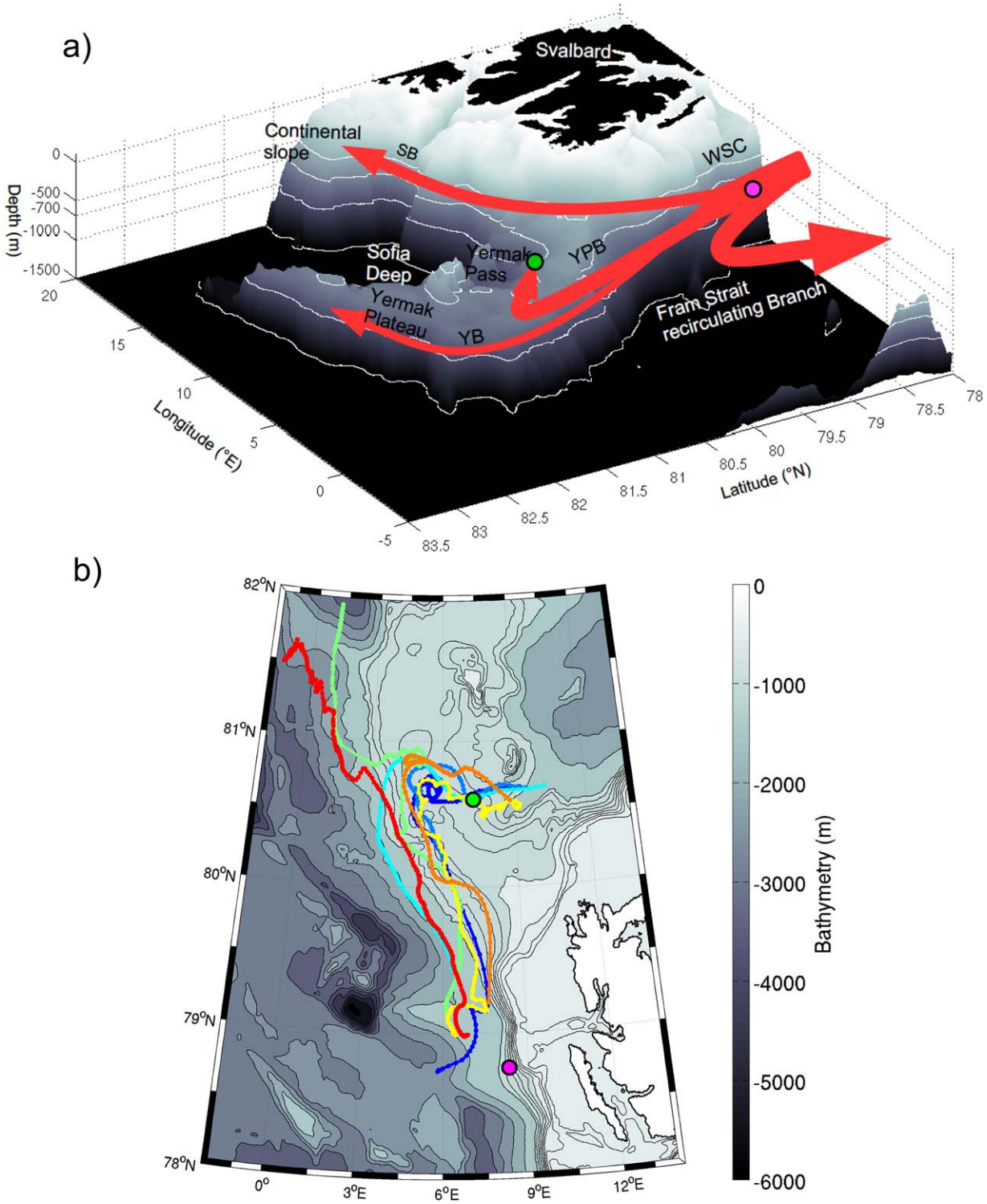

Figure 1. (a) 3-D schematic of the AW water inflow north of Svalbard. The red arrows represent the pathways of the Atlantic Water across and around the Yermak Plateau. WSC, West Spitsbergen Current; SB, Svalbard Branch; YB, Yermak Branch; YPB, Yermak Pass Branch. The white lines are the 500, 700, 1,000, and 1,500 m isolines. (b) Trajectories of the 310–340 m floats that were deployed in fall 1988 north of Svalbard and drifted through the Yermak Pass (Gascard et al., 1995). The magenta dot indicates the location of mooring F2 from the Fram Strait mooring array and the green dot the location of the mooring in the Yermak Pass. Background is the bathymetry from IBCAO (http://www.ngdc.noaa.gov/mgg/bathymetry/arctic/arctic.html). Isobaths are plotted every 200 m until 1,000 m.

to the Arctic Ocean (Koenig et al., 2017). The model outputs present a branching of the WSC as sketched in Figure 1a. The volume transports of the AW inflow ($T > 2°C$) in the three branches, Svalbard Branch, Yermak Branch, and Yermak Pass Branch, exhibit large seasonal variations in phase with the WSC volume transport that almost doubles in winter compared to summer (Beszczynska-Möller et al., 2012). The Yermak Pass Branch is mostly a winter feature associated with an overflow of the strong winter WSC (Koenig et al., 2017). Although the eddy-permitting model (4–5 km grid) does not fully resolve the Rossby radius of deformation in this area (6–8 km; Nurser & Bacon, 2013; Zhao et al., 2014), outputs point out to a large mesoscale activity and a flow in form of pulses in the branches over and around the Yermak Plateau, and along the continental slope in agreement with observations (e.g., Gascard et al., 1995; Hattermann et al., 2016; Kawasaki & Hasumi, 2016; Koenig et al., 2016; Våge et al., 2016).

The objective of the work presented here is to reexamine the flow through the Yermak Pass taking advantage of (1) the yet unpublished yearlong current time series from a mooring deployed in the middle of the Yermak Pass from July 2007 to September 2008 (Figure 1) and (2) the 10 year (2007 to present) outputs from the Mercator-Ocean global operational model. The northern location of the mooring, almost covered by sea ice during the entire year, makes this data set unique and the realistic operational model outputs help putting the yearlong point measurements in a larger spatial and temporal context.

The paper is organized as follows. Section 2 presents the mooring data, environmental context, and the model outputs used. Section 3 describes the statistics and spectral content of the velocity time series. Tides appear as a major contributor to velocity variations. We removed the dominating high frequency signals with periods less than 2 days and focused on lower frequency variations. In section 4, the model outputs are shown to have skills in representing low-frequency velocity variations in Fram Strait and in the Yermak Pass. The model outputs are then used to examine the variations in the AW inflow in the WSC and in the different branches downstream. Section 5 summarizes and discusses the results.

2. Data and Environmental Context

2.1. Yermak Pass Mooring Data

The mooring was deployed on 25 July 2007 from the *R/V Haakon Mosby* at 80.601°N, 7.119°E (depth of 745 m; green dot in Figure 1). It comprised an upward-looking RDI 75 kHz Long Ranger Acoustic Doppler Current Profiler (ADCP) at 585 m with 16 m vertical resolution and a 1 h sampling time, and an ocean profiler on a taut cable between 130 and 530 m (Gascard et al., 2017). The mooring was recovered on 23 September 2008 by the *K/V Svalbard*. The profiler did not record any data and the ADCP provided velocity data over more than a year. There are no simultaneous temperature data except for those presented in Fer et al. (2010) that were obtained during the deployment cruise. The mooring is located between stations 2 and 3 described in Fer et al. (2010). These stations indicate the presence of Atlantic Waters up to 25 m (Fer et al., 2010, their Figure 4).

Figure 2 displays the raw data from the ADCP, after declination correction. A white shaded zone is visible in the data between 380 and 500 m depth throughout the time series. It corresponds to the reflection of the acoustic bins on the profiler stuck on the cable. We ignored the data between 377 and 505 m which are polluted by the profiler reflection. The upper 90 m are not sampled and data are often missing above 200 m especially during summer. The vertical extent of the data is probably limited by the steep pycnocline between the Atlantic and Polar Surface Waters. The scarce hydrological observations around this location document variable depths for the steep pycnocline (e.g., 25 m in Fer et al., 2010 and 150 m in Meyer et al., 2017a). In particular, at the beginning of the time series, in July 2007, the ADCP provides data up to 90 m in concordance with the shallow pycnocline observed during the deployment cruise (25 m, Fer et al., 2010). The velocity time series at 570 m is complete. The percentage of available data decreases upward and varies with season (Figure 2b). In summer (April–September), more than 50% of data missing are in the upper 150 m while time series below 300 m are complete. In winter (October–March), only 35% of the data are missing at 150 m, while data gaps propagate quite deep with still 5% of missing data at 300 m. Mean velocity component profiles (Figure 2c) differ from summer to winter. In summer, current is orientated northwest, while in winter it is northeast. Means and standard deviations of velocity components and amplitude at different depths and with several length low-pass filtering are gathered in Table 1.

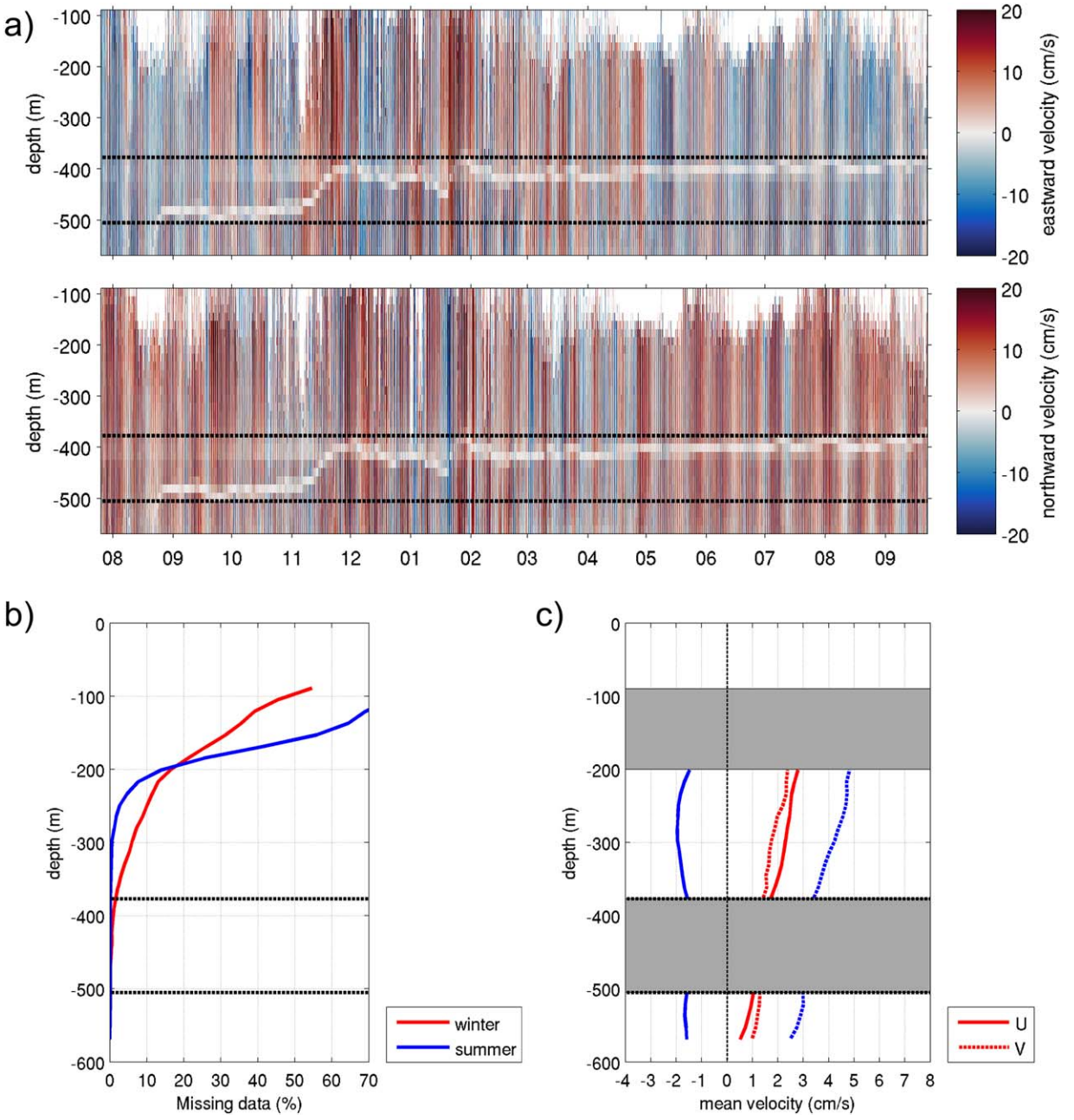

Figure 2. (a) Raw velocity time series from the ADCP in the Yermak Pass from 25 July 2007 to 23 September 2008. (top) Eastward velocity and (bottom) northward velocity (hourly resolution). *x* axis is time in months. The shadow of the profiler shows up as a white feature between 505 and 377 m. The black dashed lines delimitate the bins affected by the acoustic shadow of the profiler. (b) Percentage of missing ADCP data as a function of depth, during winter in red and summer in blue. (c) Mean velocity profiles (in cm/s). In red: winter and in blue: summer. Thick lines: eastward component and dashed lines: northward component. The grey area is the depth not analyzed in the study because of the shadow of the profiler or of the lack of data.

2.2. Ice Cover and Atmospheric Surface Conditions at the Mooring Location

The mooring was deployed a few kilometers from the ice edge and was recovered in the middle of ice floes. Sea-ice concentration from AMSR-E data (daily, 12.5 km spatial resolution, https://nsidc.org/data/amsre) indicates that the mooring was under sea ice 10 months out of 12 (Figure 3b). The mooring was located north of the mean position of the ice edge (Figure 4). Note that in this region, the ice edge is shifted further south in summer than in winter (Figure 4).

Era-Interim reanalysis outputs (Dee et al., 2011) were used to document atmospheric surface conditions at the mooring location. Wind intensity (Figure 3c) and surface temperature (not shown) feature a large

Table 1
Mean (cm/s) and Standard Deviation (in Parentheses; cm/s) of Velocity Time Series at Different Depths (570, 300, and 250 m) and Different Seasons From the ADCP

		Total			Summer			Winter		
cm/s		U	V	Amplitude	U	V	Amplitude	U	V	Amplitude
570 m (100%)	Full	−0.7 (8.5)	1.8 (8.2)	10.5 (5.6)	−1.4 (7.6)	2.4 (7.5)	10.0 (4.9)	0.5 (9.4)	1.0 (8.9)	11.3 (6.3)
	50 h	−0.67 (3.7)	1.8 (3.3)	4.6 (2.7)	−1.4 (2.1)	2.4 (2.0)	3.6 (1.7)	0.5 (4.7)	1.0 (4.1)	5.5 (3.2)
	20 days	−0.68 (2.1)	1.9 (1.9)	3.0 (1.8)	−1.4 (1.2)	2.3 (9.0)	2.9 (1.0)	0.5 (2.3)	1.0 (1.8)	2.7 (1.6)
300 m (97%)	Full	−0.2 (9.5)	3.2 (9.5)	12.3 (6.3)	−1.9 (8.0)	3.9 (8.6)	11.4 (5.3)	2.3 (10.8)	1.8 (10.5)	13.6 (7.2)
	50 h	−0.15 (5.5)	3.1 (4.8)	7.0 (3.7)	−1.9 (3.4)	4.0 (3.9)	6.2 (2.9)	2.2 (6.6)	1.7 (5.6)	8.0 (4.4)
	20 days	0.13 (4.1)	3.2 (2.9)	5.2 (2.7)	−1.9 (2.3)	3.9 (2.4)	5.1 (2.1)	2.2 (4.7)	1.7 (2.8)	5.2 (3.4)
250 m (94%)	Full	−0.05 (9.9)	3.7 (10.0)	12.9 (6.7)	−2.0 (8.2)	4.3 (8.8)	11.6 (5.5)	2.5 (11.5)	2.2 (11.2)	14.5 (7.8)
	50 h	−0.05 (6.0)	3.5 (5.2)	7.6 (4.1)	−2.0 (3.6)	4.3 (4.2)	6.5 (3.2)	2.5 (7.2)	1.9 (6.1)	8.7 (4.9)
	20 days	−0.06 (4.5)	3.5 (3.0)	5.7 (3.0)	−2.0 (2.5)	4.3 (2.6)	5.4 (2.3)	2.7 (5.2)	2.0 (3.0)	5.7 (3.7)

Note: The percentage is the percentage of available data at each depth over the time series. U, eastward velocity; V, northward velocity; Total, July 2007 to September 2008; Winter, October 2007 to March 2008; Summer, April 2008 to September 2008; Full, full-time resolution time series; 50 h, time series filtered with a 50 h low-pass Butterworth filter; 20 days, time series filtered with a 20 day low-pass Butterworth filter.

seasonal cycle with distinct signature of strong synoptic events in winter. The wind speed shows larger mean and standard deviation from October to March (winter; mean 8.7 m/s, standard deviation [std] 3.7 m/s) than from April to September (summer; 5.5 and 2.7 m/s). Surface temperatures are positive from June to September and reach values below −20°C from December to April (not shown). A succession of storms is observed from October to March with velocities in excess of 15 m/s associated with temperature peaks and sea level pressure drops (below 980 hPa on several occasions, not shown).

2.3. Tidal Model and Ocean Operational Model

We used the Arctic Ocean Tidal Inverse Model (AOTIM-5; Padman & Erofeeva, 2004) to estimate the tidal current velocities associated with the eight most energetic tidal components (M_2, S_2, N_2, K_2, O_1, K_1, P_1, and Q_1) at the mooring location (Figure 3d). The model provides barotropic tidal velocities on a 5 km horizontal resolution grid. The model current speeds are large with values exceeding 20 cm/s and exhibit a striking fortnightly modulation corresponding to the beat period between O_1 and K_1. The fortnightly oscillations constitute the upper and lower envelope of the diurnal variations (Figure 3d). A visual comparison with the current speeds observed at the deepest bin of the ADCP (570 m; Figure 3e) suggests that AOTIM-5 model performs rather well and that tides dominate the velocity signal.

We also examined operational ocean model daily outputs to put the mooring data in a continuous and larger spatial and temporal 2007–2016 context. The model is the global ocean operational model system developed at Mercator-Ocean for the Copernicus Marine Environment Monitoring Service (CMEMS; http://marine.copernicus.eu/), with a 1/12° horizontal resolution and z-50 vertical levels. The system is based on the NEMO (Nucleus for European Modelling of the Ocean; Madec & NEMO Team, 2008) platform and uses a multidata and multivariate reduced order Kalman filter based on the Singular Extended Evolutive Kalman (SEEK) filter formulation introduced by Pham et al. (1998). The model uses the LIM2 thermodynamic-dynamic sea-ice model and is driven at the surface by atmospheric analysis and forecasts from the IFS (Integrated Forecasting System) operational system at ECMWF (European Centre for Medium-Range Weather Forecasts). The assimilated observations are along-track satellite altimetry, sea surface temperature (SST), and in situ vertical profiles of temperature and salinity. The data assimilation scheme is fully operational for SST warmer than −1°C and is switched off for SST colder than the freezing point (in ice-covered areas). Sea-ice concentration derived from IFREMER/CERSAT satellite data (Ezraty et al., 2007) is assimilated in this version of the model. Full description of the system components is available in Lellouche et al. (2012). The system starts in October 2006 from a "cold" start (initial currents are null) and from World Ocean Atlas 2013 global temperature and salinity climatology. The model outputs are compared to the mooring F2 of the Fram Strait mooring array in the core of the WSC at 78.4°N (magenta dot in Figure 1; Beszczynska-Möller et al., 2015). Comparisons, presented in section 4, are rather satisfactory (the mooring data are not assimilated).

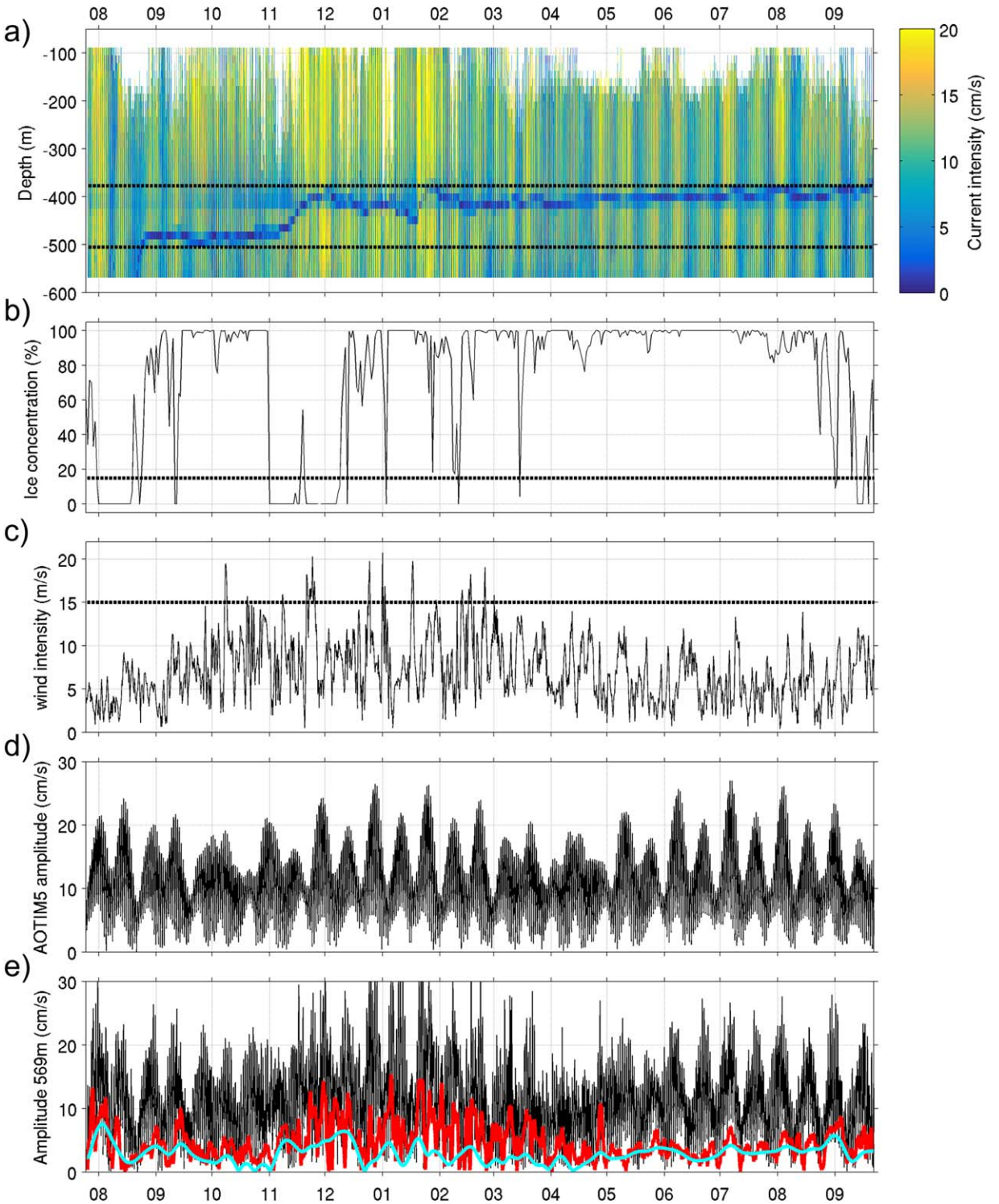

Figure 3. Time series of several variables at the mooring location. (a) Current speed from 580 to 90 m (in cm/s) deduced from the ADCP (hourly resolution). *x* axis is time in months. The black dashed lines delimitate the bins affected by the acoustic shadow of the profiler. (b) Ice concentration (%) from AMSR-E satellite data, 1 day time resolution and 12.5 km spatial resolution. The dashed line highlights 15% concentration, usually considered as the ice edge. (c) Wind intensity (m/s), 6 h resolution, from Era-Interim reanalysis. The dashed line (15 m/s) can be considered as a criterion for storms. (d) Barotropic tide current speed (in cm/s) deduced from AOTIM5 model (Padman & Erofeeva, 2004). (e) ADCP current speed at 570 m (in cm/s), in black: full-time resolution (hourly), in red: filtered with a 50 h low-pass Butterworth filter, and in blue: filtered with a 20 day low-pass Butterworth filter.

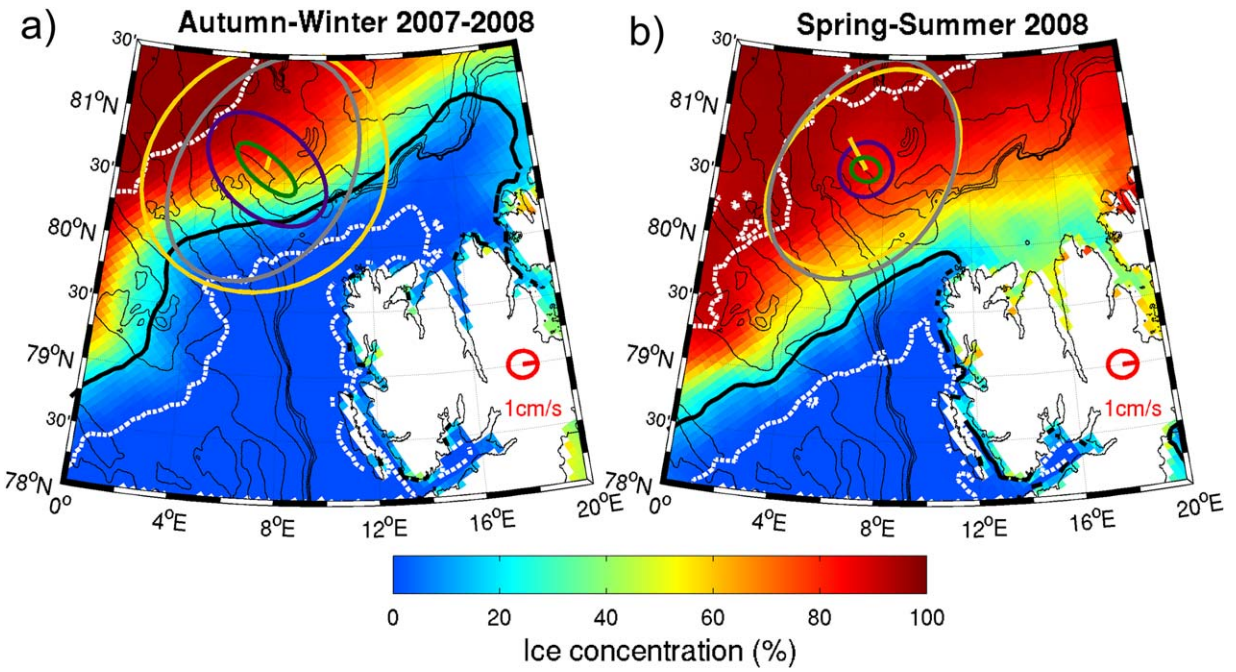

Figure 4. Background is sea-ice concentration (in %) from AMSR-E averaged over (a) October 2007 to March 2008 (autumn/winter) and (b) April–September 2008 (spring/summer). The thick black line is the mean sea-ice edge (defined as the 15% sea-ice contour) over the corresponding period. The thick dashed white lines are respectively the southernmost sea-ice edge and the northernmost sea-ice edge at each longitude. On each map, means and ellipses of variances of the 570 m depth in situ velocity data and of the AOTIM-5 velocity at the corresponding season are plotted: the AOTIM-5 velocity outputs in grey, the velocity observations full-time resolution in yellow, 50 h low-pass filtered observations in blue, and 20 day low-pass filtered observations in green. The red arrow and ellipse of variance show the scale. The thin black lines are bathymetry contours (500, 600, 700, 1,000, 2,000, and 3,000 m).

3. Statistics and Spectral Content of the In Situ Velocities

3.1. Full-Time Resolution Time Series: High Frequencies at 570 m Depth

The ADCP current speed time series shows large high frequency variations with a conspicuous semimonthly periodicity and higher frequencies (Figure 3a). Barotropic tides are a major contributor to velocity fluctuations and current speeds at 570 m, the deepest observed level (mean 10.5 cm/s and std 5.65 cm/s), compare rather well with the AOTIM-5 tide prediction (mean 10 cm/s and std 4.75 cm/s; Figures 3d and 3e). The barotropic tide from AOTIM-5 model represents 73% of the variance of the northward component, and 97% of the eastward component. Overall correlation between the 570 m velocity and the model tide-induced current speed time series is 0.63. Correlation is modulated over the year with larger correlation in spring/summer ($r = 0.78$ in summer 2008) than in autumn/winter ($r = 0.57$).

The ellipses of variance of the full-time resolution ADCP velocity at 570 m are compared with the ellipses of variances of the AOTIM-5 current (Figure 4). In spring/summer, the ellipses of variance of the current data and of the AOTIM-5 model agree remarkably well in intensity and direction (std along the main axis orientated across-bathymetry 9.1 cm/s, Figure 4b). The main current forcing in summer is the tide. The mean current in summer (2.8 cm/s to the northwest along the slope Figure 4b) can be interpreted as a residual current due to the tide rectification, a superposition of Coriolis and frictional processes over steep topography (Padman et al., 1992; Polton, 2015). In autumn/winter, the ellipse of variance of the current data is larger than the ellipse of variance from AOTIM-5 (std along the main axis 9.7 cm/s in the current data versus 9.1 cm/s in the AOTIM-5 model; along the secondary axis: 8.4 cm/s versus 6.4 cm/s respectively, Figure 4a). In autumn/winter, other processes than the tide affect the current at 570 m and the mean current is small (1.1 cm/s) across-bathymetry to the northeast (Figure 4a). For the sake of estimating an order of magnitude, if we suppose that the residual tidal current is the same in winter as in summer, the other processes are responsible for a mean current to the southeast of about 2.4 cm/s at 570 m.

Rotary spectra (clockwise [CW] figures on the left and counterclockwise [CCW] figures on the right, Figure 5) of the in situ velocity at 570 m confirm the dominance of diurnal and semidiurnal periods (Figure 5a). The

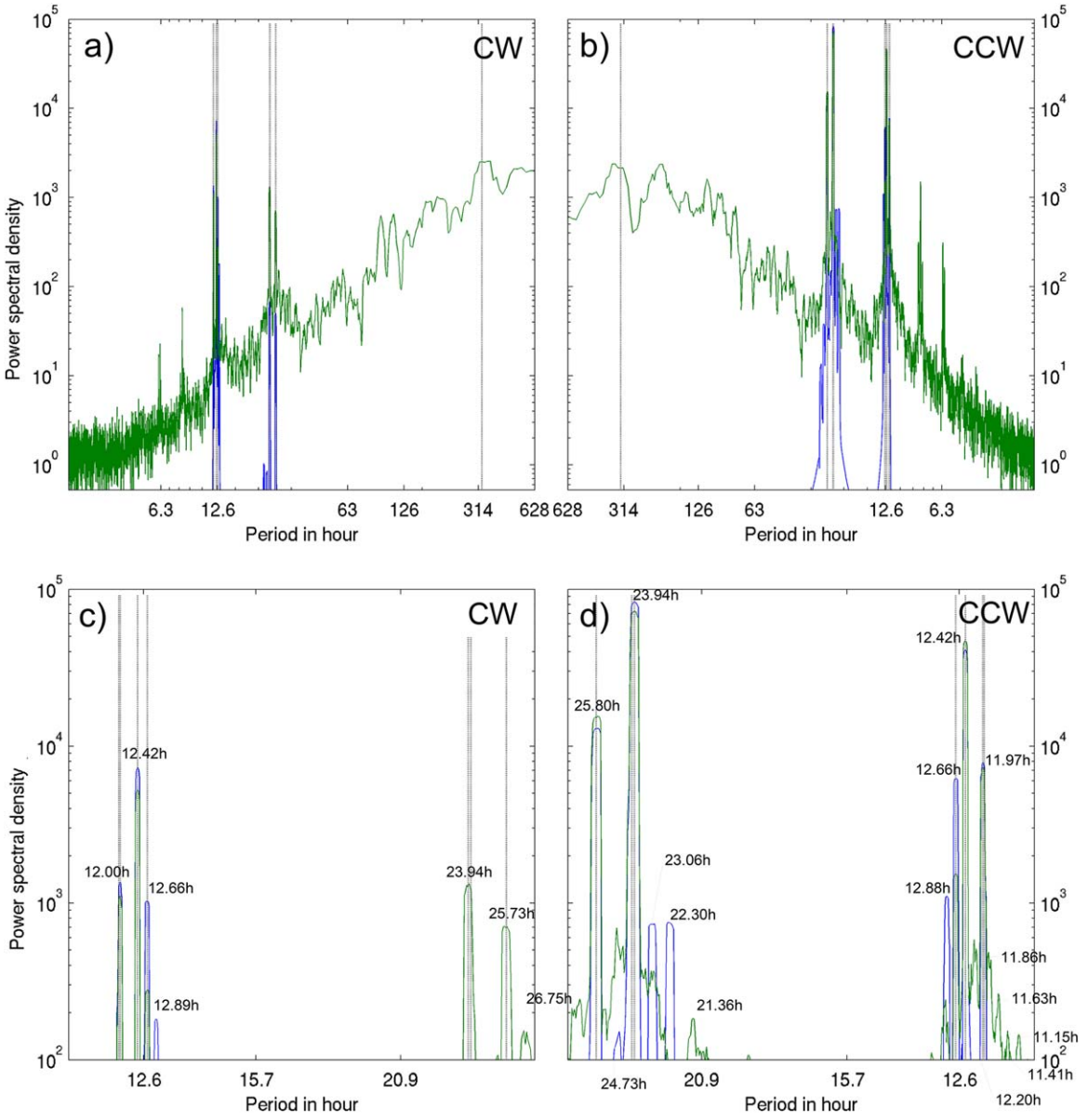

Figure 5. (a, b) Rotary spectra of the velocity time series at 570 m (in green) and of the AOTIM5 model time series (in blue). We use a seven lowest order Slepian tapers with a time-bandwidth product of 4. (a,c): negative/clockwise (CW) rotary spectrum. (b, d): positive/counterclockwise (CCW) rotary spectrum. The *x* axis is period in hour, the *y* axis is energy (in cm/s^2). The black vertical dashed lines correspond to the dominant periods in tide signal: four peaks around 12 h (11.96, 12, 12.4, and 12.6 h), three around 24 h (23.93, 24.06, and 25.8 h), and one at 328 h (13.6 days). The near-inertial period (12.12 h) at the mooring location cannot be distinguished from the tidal period. (c, d) Close-up of the rotary spectra over the semidiurnal and diurnal periodicity. CW, clockwise; CCW, counterclockwise. Same color code and axis as in Figure 5a.

dashed lines on the rotary spectra indicate tide component periods, with four periods composing the semidiurnal signal (K_2 at 11.97 h, S_2 at 12.00 h, M_2 at 12.42 h, and N_2 at 12.66 h), four periods for the diurnal signal (K_1 at 23.93 h, P_1 at 24.07 h, O_1 at 25.82 h, and Q_1 at 26.87 h), and a period at 13.66 days (325 h), the fortnightly tide period, corresponding to the beat between O_1 and K_1 (Kowalik & Luick, 2013 and Figure 5). The near-inertial period at the mooring location is 12.13 h, very close to the semidiurnal tide periods.

The most energetic peaks in the rotary spectra of the data and of the AOTIM-5 model are M_2 (12.42 h) for the semidiurnal signal and K_1/P_1 (23.94 and 24.07 h, not distinguishable in the rotary spectra of the ADCP deep velocity time series) for the diurnal signal. Energy peaks of AOTIM-5 at the main diurnal and semidiurnal tide components in both CW and CCW figures compare well with the in situ current (difference of less

than a factor 2). There are differences in the amplitude of the secondary peaks between in situ and AOTIM-5 velocity spectra, especially in the CCW figure. Several causes can be at the origin of those differences: first bathymetry in the AOTIM-5 model may not be accurate. Then, other signals are probably present in the in situ data, such as internal waves and near-inertial waves.

The main signal in the CCW figure is the diurnal signal, in agreement with Padman and Dillon (1991). In the CW figure, the semidiurnal signal dominates in both in situ data and in the AOTIM-5 model, probably the result of reflections of the barotropic tide on the bathymetry. The ratio of CW/CCW energy in the diurnal and semidiurnal band (1 order of magnitude, not shown) indicates that the tide has mainly an upward propagation signature. Less energetics peaks in both the CCW and CW spectra of the velocity are observed at higher frequencies (periods around 8.2 and 6.2 h) are harmonics of the diurnal and semidiurnal signals. The fortnightly period (13.66 days), the striking signal in the current data and in the AOTIM-5 current speed (Figures 3d and 3e) does not appear in the AOTIM-5 rotary spectra as it is a beat. Further analysis of the tide (e.g., baroclinic tides) and other high frequency signals (e.g., internal waves) is beyond the scope of this paper.

3.2. Mesoscale Features: Period Less Than 20 Days

The large tidal signal was removed from the velocity component time series with a 50 h low-pass Butterworth filter. The amplitude of variations is then much reduced (e.g., red curve in Figures 3e and 4 and Table 1). Means and ellipses of variance vary with season and depth (Table 1 and Figure 6). In Figure 6, the data gaps at 300 and 250 m, respectively 3% and 6% of the time series, are filled with the value of the upper available observation in the water column. In winter, the mean current rotates cyclonically with increasing depth, while the main axis of the ellipses rotates anticyclonically. In summer, ellipses are smaller and the mean velocities and the main axes of the ellipses have the same direction toward the northwest parallel to isobaths and decrease in amplitude with increasing depth. The velocity structure is barotropic equivalent in summer while it shows baroclinicity in autumn/winter.

Spectra of the along-bathymetry component of the 50 h low-pass filtered velocity time series at 570 and 300 m show several salient peaks above the 95% confidence level in the range of periods from 3.4 to 50 days (Figure 7). Energy levels are twice smaller at 570 m than at 300 m. Prominent peaks at 4.6, 9.2, and 13 days in the core of the Atlantic Water (300 m) can be signature of mesoscale activity. Indeed, the

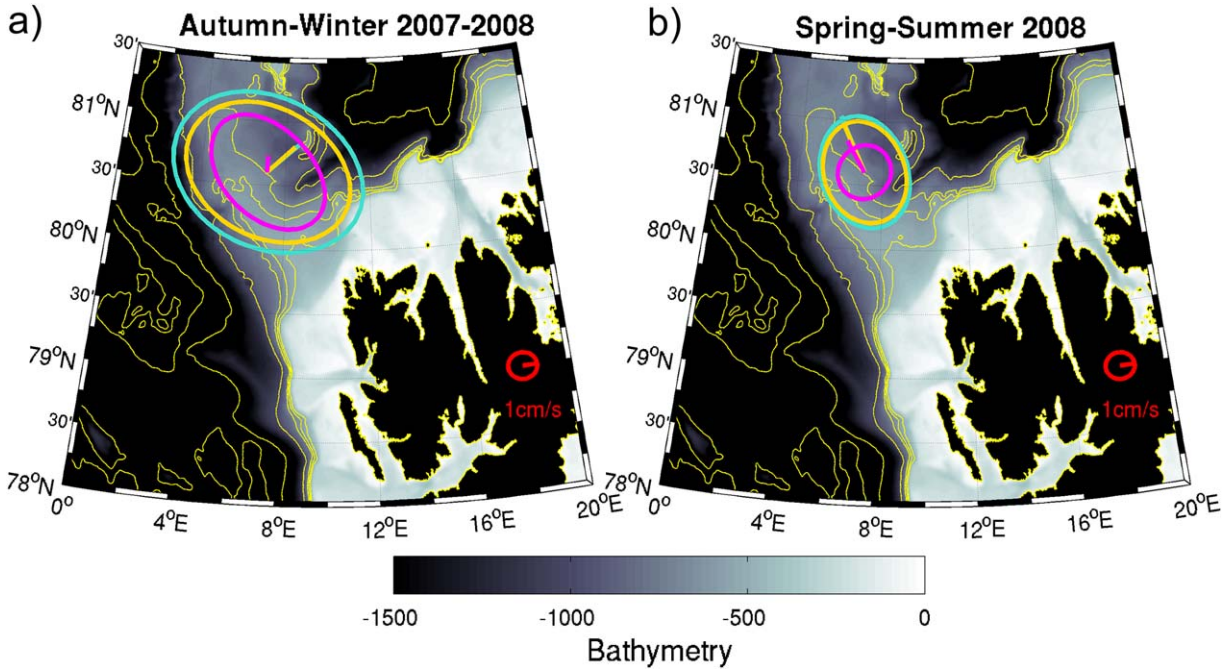

Figure 6. Means and variance ellipses of the in situ velocity data filtered with a 50 h low-pass Butterworth filter at several depths—magenta: at 570 m, yellow: at 300 m, and blue: at 250 m. The red arrow and ellipse of variance are the scale. Background is bathymetry, the thin yellow lines are bathymetry contours.

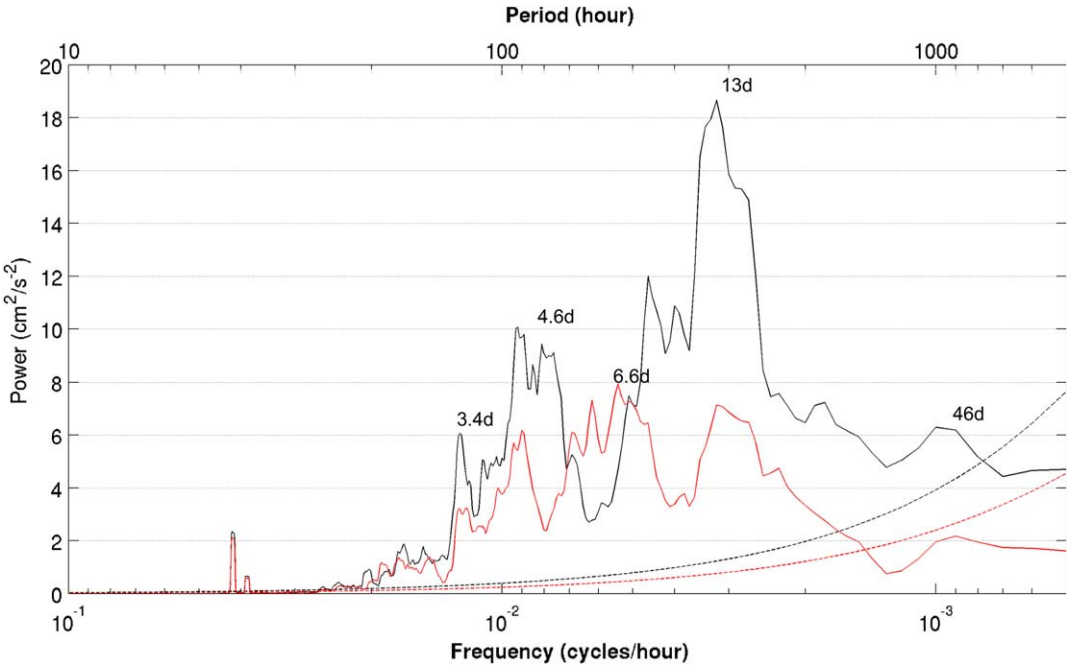

Figure 7. Variance-preserving spectra of the along isobath component velocity at 570 m (red) and 300 m (black) from the ADCP filtered with a 50 h low-pass Butterworth filter (by averaging over groups of 10 adjacent frequencies). The dotted lines show the 95% confidence level against the red noise background from a first-order autoregressive (AR1) process. The *y* axis is the power in cm^2/s^{-2}. The *x* axis is (bottom) frequency labeled in (top) period. The periods of the most energetic peaks are indicated in days.

ARCTEMIZ88 drifting floats that proceeded through the Yermak Pass (Figure 1b) documented vortices with rotating timescales from 5 to 15 days, curvature radius of about 4 km and tangential speeds of 10 cm/s (Gascard et al., 1995; Richez, 1998).

3.3. Seasonal Variations

We applied a 20 day low-pass Butterworth filter to the ADCP velocity components (Table 1). At 570 m, mean current and variance ellipse are small (Table 1 and Figure 4 in green). At 300 m depth, in the core depth of the Atlantic Water inflow (Fer et al., 2010), means remain small and ellipses are larger (Figure 8, yellow). In summer (April–September), the mean current at 300 m is about 4.3 cm/s to the northwest along the 700 m isobath and the ellipse is circular with an std around 2.4 cm/s (Figure 8a). In winter (October–March), the mean current at 300 m is orientated across-bathymetry to the northeast (2.6 cm/s), the ellipse has a main axis (std 4.9 cm/s) along bathymetry. Note that the winter mean and ellipse at 300 m are comparable to those deduced from the ARCTEMIZ88 floats (Richez, 1998). If we suppose that the summer mean velocity at 300 m (4.3 cm/s to the northwest along the slope, Figure 8b yellow arrow) is essentially due to tide or eddy rectification and that the residual current is the same in winter as in summer, then a mean flow of 4.7 cm/s to the southeast is necessary to produce the winter mean of 2.6 cm/s to the northeast (Figure 8a, yellow vectors). This is just an order of magnitude because of the questionable hypothesis of a same residual current in winter and summer. The mean value of 4.7 cm/s in the AW core in winter is larger than the 2.4 cm/s estimated at 570 m (section 3.1; dashed yellow arrow in Figure 8a to the southeast).

The spectrum of the velocity component parallel to the main axis of the ellipse of variance shows two peaks, at 32 and 70 days (Figure 9, black curve). These peaks could correspond to monthly/bimonthly velocity pulses of current in the Yermak Pass Branch. The mean velocity during velocity pulses, defined as 20 day low-pass filtered currents with a speed larger than 10 cm/s, is eastward along the downstream bathymetry, almost parallel to the north coast of Svalbard (Figure 8a, green arrow). During the velocity pulses, ADCP data reach up to 90 m suggesting that the pycnocline shallows to less than 90 m from the surface (Figures 2a and 3a) and that the warm AW flows through the pass and extends closer to the surface with potential

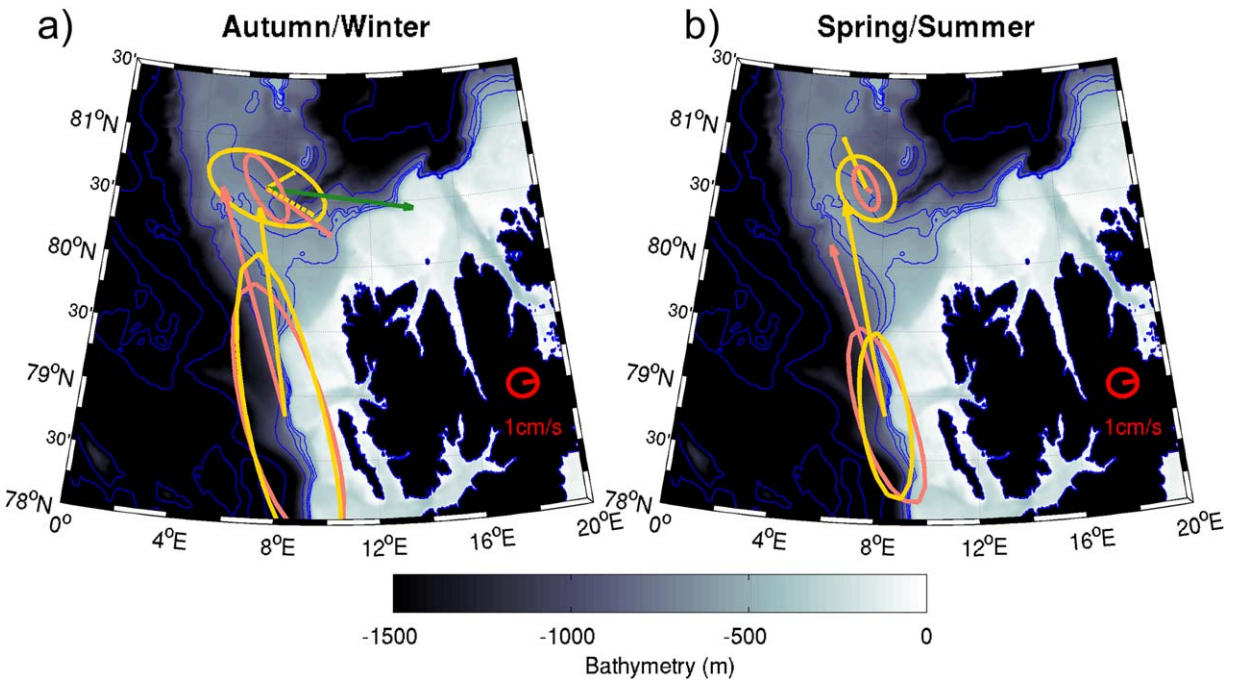

Figure 8. Velocity means and variance ellipses of model outputs (full salmon lines) and in situ data (full yellow lines) at the location of the ADCP mooring at 300 m and mooring F2 in Fram Strait at 250 m (a) in summer (April–September) and (b) in winter (October–March). The ADCP mooring data are 20 day low-pass filtered with a Butterworth filter, the currentmeter data in Fram Strait are 10 day low-pass filtered with a Butterworth filter. In winter, the green arrow in the Yermak Pass features the composite for in situ 20 day low-pass filtered current speeds larger than 10 cm/s. The yellow dashed vector is the mean velocity current once the estimated tide residual current is removed. The red arrow and ellipse is the scale. Background is bathymetry (in m). The blue isolines are 3,000, 2,000, 1,000, 800, 700, 600, and 500 m.

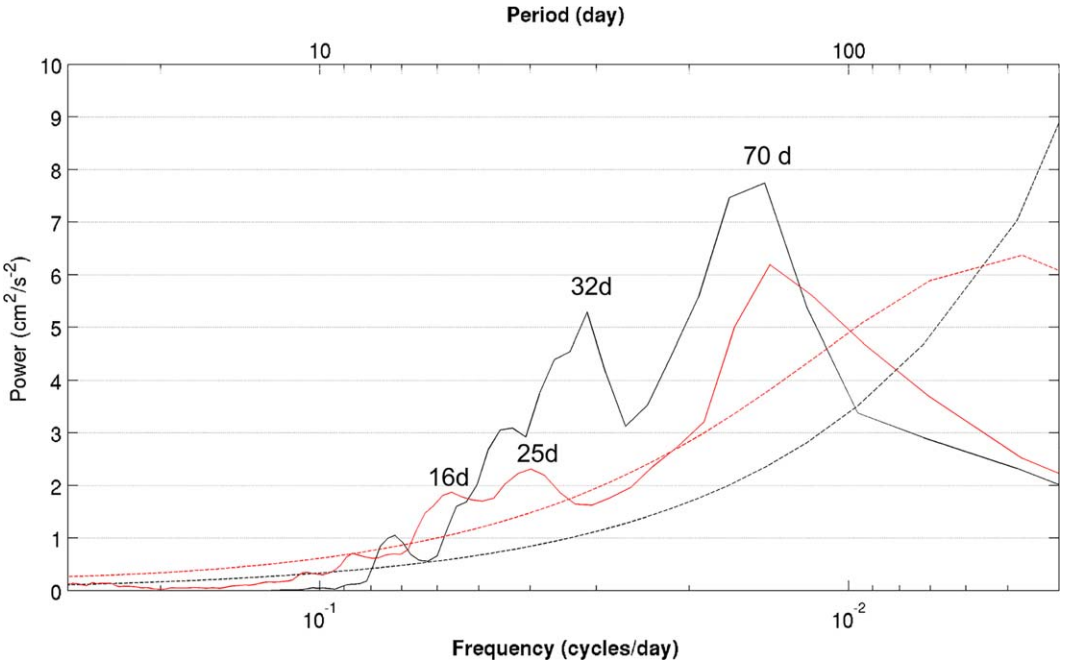

Figure 9. Variance-preserving spectra. In black: the velocity component along isobath at 300 m from the ADCP filtered with a 20 day low-pass Butterworth filter (by averaging over groups of four adjacent frequencies). In red: the along-isobath velocity at 266 m from the model outputs at the Yermak Pass mooring location (by averaging over groups of 12 adjacent frequencies). The dotted lines (red/black) show the 95% confidence level against the red noise background from a first-order autoregressive (AR1) process (from the ADCP data/the model outputs respectively). The *y* axis is the power in cm^2/s^{-2}. The *x* axis is (bottom) frequency labeled in (top) period.

impact on the ice cover. Indeed, the mooring is ice-free during several months in autumn-winter while it is ice covered in summer (Figure 3b).

The ADCP current data confirm the strong seasonality of the Yermak Pass Branch, which is mostly a winter pattern as Mercator-Ocean operational model outputs suggested (Koenig et al., 2017). The eastward flow of Atlantic Water through the Yermak Pass in winter seems to occur in episodes of intense flow (velocity larger than 10 cm/s) of 1–2 month periodicity. In the next section, we use 10 years of outputs from the operational Mercator-Ocean model to examine the Yermak Pass Branch variations.

4. AW Inflow North of Svalbard in Mercator-Ocean Operational Model Outputs

4.1. Model Performances in Fram Strait and in the Yermak Pass

Koenig et al. (2017) showed that the 1/12° resolution Mercator-Ocean global operational model reproduces reasonably well seasonal cycles in volume transports and temperatures of the AW inflow at Fram Strait (comparison with the 13 years statistics, 1997–2010, from Beszczynska-Möller et al., 2012) and at 30°E and 81.8°N (comparison with mooring statistics from Ivanov et al. (2009), and temperatures from NABOS data http://nabos.iarc.uaf.edu). Comparisons with contemporary winter hydrographic data from the IAOOS platform drift north of Svalbard during N-ICE2015 experiment also showed a remarkable agreement (Koenig et al., 2017). Here we proceed to a more detailed comparison with the currentmeter data at 250 m from mooring F2 (magenta dot Figure 1) located in the core of the WSC in Fram Strait (78.84°N, 8.33°E) for the period 2007–2009 (Beszczynska-Möller et al., 2012).

Mean and standard deviation are in very good agreement between the 10 day low-pass filtered in situ data at F2 and the collocated daily model outputs. The mean current, around 12 cm/s in summer and 16 cm/s in winter, flows along the bathymetry. The ellipses are elongated in the northward direction in summer and winter, and are of the same order of magnitude (7 cm/s in summer and 10 cm/s in winter, Figure 8). Time variations of the northward velocity of the in situ data (F2) and the model outputs are significantly correlated ($r = 0.34$) in spite of the large eddy activity of the WSC (Hattermann et al., 2016; Von Appen et al., 2016). Temperature variations in the model outputs and at F2 are highly correlated ($r = 0.75$), with a modeled negative bias of 0.04°C and a root-mean-square error of 0.38°C. Temperature time series (not shown) feature a large seasonal cycle with a maximum at the end of summer/beginning of fall (4.5–5°C in October 2008) and a minimum at the end of winter/beginning of spring (2–2.5°C in April 2008). The inflow of the Atlantic Water in the Arctic is well represented in the model.

At the mooring location over the Yermak Plateau (green dot in Figure 1), mean currents from the model outputs differ from the 20 day low-pass filtered in situ data in several ways. In summer, the modeled mean current is weak (0.5 cm/s) and orientated southeast (4.3 cm/s to the northwest for the in situ data; Figure 8b). In winter, the modeled mean current in the model outputs is orientated southeast (mean 6.3 cm/s) along bathymetry whereas it is orientated across-bathymetry in the in situ data (Figure 8a). Differences are probably due to the fact that the model does not represent tides. Indeed, the in situ mean velocity comprises a nonlinear residual tide component. The model mean of 6.3 cm/s to the southeast is comparable with the mean value (4.7 cm/s to the southeast) obtained by removing the tide-induced residual velocity estimate from the mean observed velocity (see section 3.3; Figure 8a, dashed yellow and salmon vectors).

The model does show skills in representing seasonal variations of the Yermak Pass Branch with a smaller variance ellipse in summer than in winter. Eddies documented by ARCTEMIZ88 floats are small scale, about 4 km curvature radius (Richez, 1998). This scale is not fully resolved by the 1/12° resolution model outputs, the model variance ellipses are smaller than those deduced from the ADCP (Figures 8a and 8b). The spectrum of the along-bathymetry velocity component from the daily model outputs (in red) bears similarities in intensity and energized frequencies with the spectral content of the 20 day low-pass filtered in situ velocities (in black) with a significant peak at about 70 days and another one about 25 days (Figure 9). Those periods correspond to the time scales of episodes of intense flow documented in section 3.3. The daily model velocity outputs do not have energy at periods smaller than 10 days.

4.2. Model Outputs in 2007–2008: Local Circulation and Links Between the YPB and the WSC

Figure 10 shows the mean currents around the mooring location (Yermak Pass, black dot) from the model outputs at 266 m depth in autumn/winter 2007–2008 (Figures 10a and 10c) and spring/summer 2008 (Figures 10b and 10d), in a regional map (top) and in a close-up over the Yermak Pass (bottom). The seasonality

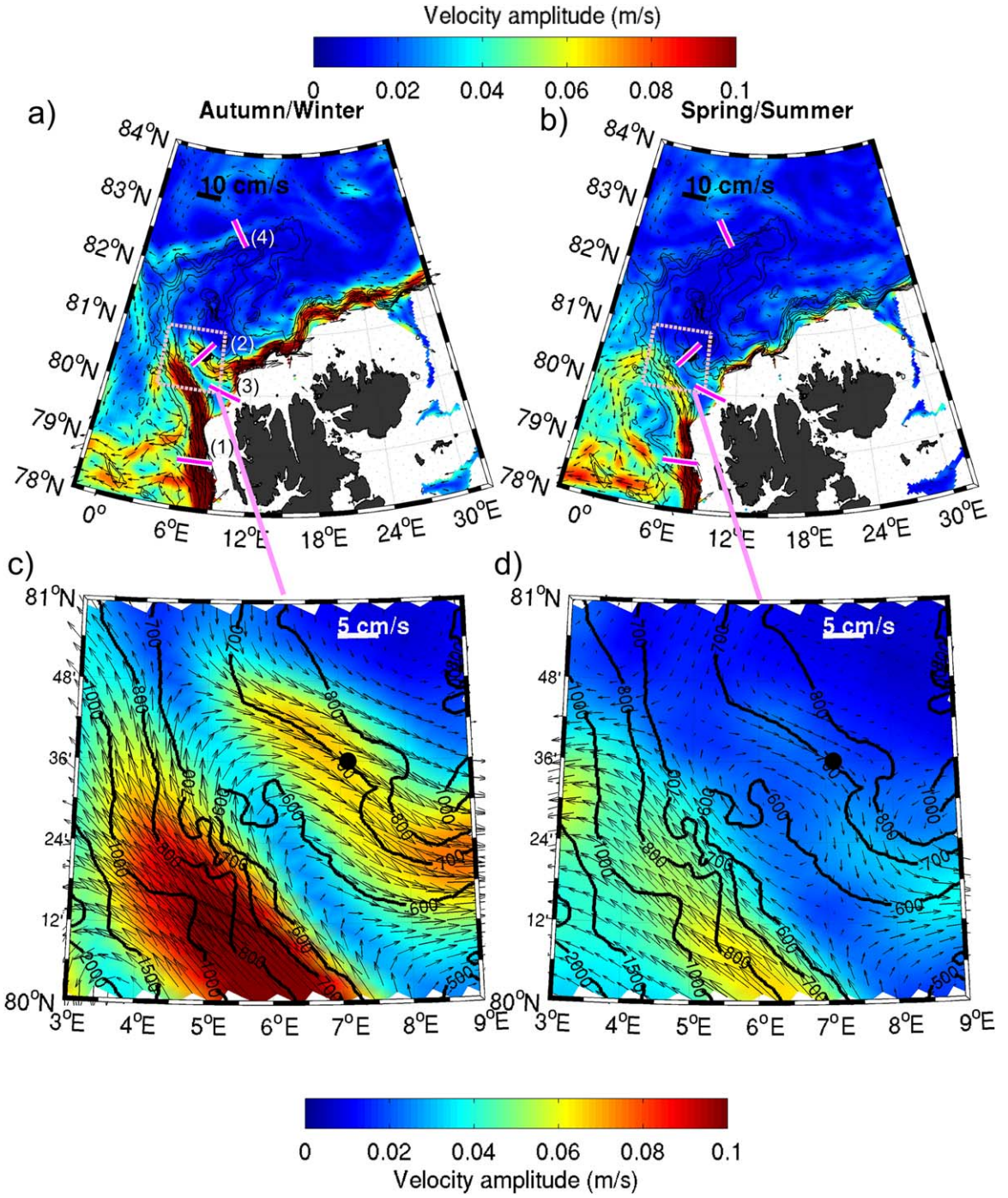

Figure 10. Mean circulation (arrows in cm s^{-1}) from the model outputs in the AW layer (50 m-thick layer centered at 266 m) over (a) winter: October 2007 to March 2008 and (b) summer: July 2007 to September 2007 and April 2008 to September 2008. The current speed smaller than 1 cm/s is not plotted. (bottom) Close-up on the mean circulation over the Yermak Pass (pink box indicated in the top). The black dot indicates the mooring location. The bathymetry contours are 500, 600, 700, 800, 1000, and 1,500 m. The magenta lines are the sections used to compute the volume transport presented in Figure 9. (1) West Spitsbergen Current (WSC) section, (2) Yermak Pass Branch (YPB) section, (3) Svalbard Branch (SB) section, and (4) Yermak Branch (YB) section.

of the current in the AW core is striking: larger flow in winter in the WSC, the Yermak Pass branch and in the eastward current along the continental slope north of Svalbard. In winter, the AW Yermak Pass Branch merges with the Svalbard Branch to the east of 10°E along the Svalbard continental slope. The Fram Strait recirculating branches are intense in both seasons. The close-up over the Yermak Pass (Figures 10c and 10d) highlights interesting features. In winter, the mean velocity exceeds 5 cm/s and the current flows

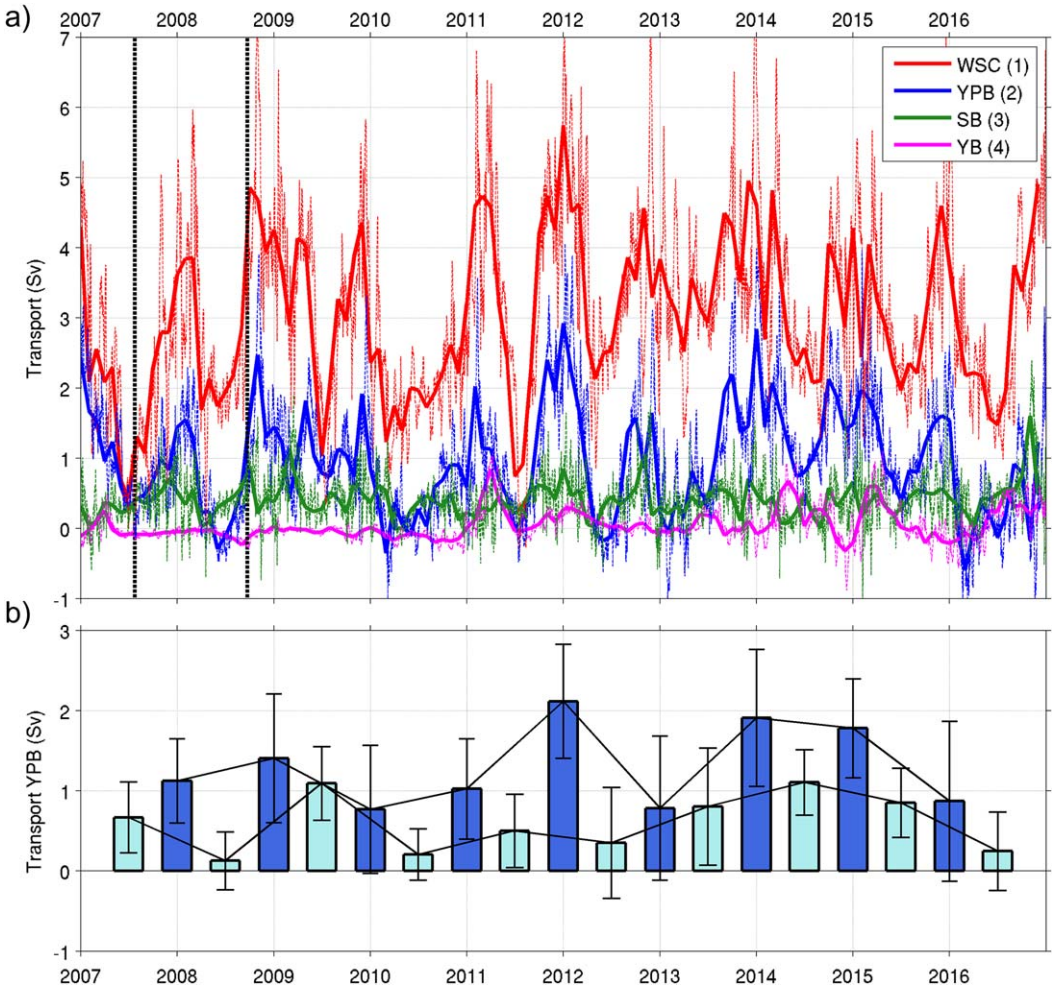

Figure 11. (a) Time series of volume transport (in Sv) of water with temperature larger than 1.5°C from model outputs through several sections presented in Figure 10. *x* axis is time in years. Dashed lines are the full-time resolution time series, thick lines are the monthly means. WSC, West Spitsbergen Current; SB, Svalbard Branch; YPB, Yermak Pass Branch; YB, Yermak Branch. The black dashed lines delimitate the period of the mooring data in the Yermak Pass. (b) Seasonal mean of the volume transport of the Yermak Pass Branch (in Sv). In dark blue: over October–March (winter). In light blue: over April–September (summer). Vertical bars are the standard deviation of daily volume transport for each season.

between the isobaths 600–800 m. In summer, the flow is narrower, between isobaths 600 and 700 m and a small recirculation is formed around the 600 m isobath contour (centered at 6.5°E, 80.5°N). The standard deviation of the intensity (not shown) does not show large variations of the current in summer, while it is large in winter along the main flow, confirming that the Yermak Pass Branch flows in pulses in winter.

The in situ northward velocity at F2 (in Fram Strait) at 250 m and the in situ current speed of the ADCP in the Yermak Pass at 300 m are barely correlated ($r = 0.16$) with a lag of 15 days. In the modeled velocities, the correlation is larger ($r = 0.33$) with a smaller lag of 6 days. Such short lags are due to the propagation of coastal trapped waves that are much faster than the mean current. The distance between the ADCP in Yermak Pass and F2 in Fram Strait along isobaths is about 300 km, which implies an order of magnitude of 60 cm/s for the propagation velocity in model outputs. The larger correlation and smaller lags between modeled velocities in Fram Strait and in the Yermak Pass compared to observations are probably due to the fact that the model misses the energetic tides in the Yermak Pass Branch and their interactions with the flow which reduce correlations with the Fram Strait inflow. Modeled temperatures at F2 and in the Yermak Pass at 266 m show a maximum correlation ($r = 0.73$) at a lag of 33 days. This lag corresponds to the time of temperature anomaly propagation of the Atlantic Water inflow with a background current velocity of 10 cm/s. (Note that there is no in situ temperature time series in the Yermak Pass.)

Table 2
Volume Transport Statistics (Sv) Across Several Sections Over the Yermak Plateau and the Svalbard Continental Slope for the Water Warmer Than 1.5°C From 2007 to 2017

		WSC	YPB	SB	YB
	Total	3	0.9	0.4	0.04
Mean	**Summer**	2.4	0.6	0.3	0.08
	Winter	3.7	1.3	0.4	0.01
	Total	1.3	0.8	0.3	0.2
Std	**Summer**	1.0	0.6	0.2	0.2
	Winter	1.3	0.9	0.4	0.2
Min		−0.3	−1.1	−1.2	−0.9
Max		7.9	4.0	2.4	1.1

Note: WSC, West Spitsbergen Current; YPB, Yermak Pass Branch; SB, Svalbard Branch; YB, Yermak Branch. In each case, the first line is the total, the second line is summer (April–September) and the third line is winter (October–March).

We now examine the evolution of the WSC and its partition downstream in the 10 years of model outputs.

4.3. Variations in the AW Inflow in the WSC and Its Partition Downstream Over 2007–2016

Volume transports of waters warmer than 1.5°C (Atlantic Water) were computed from model outputs through the 4 sections drawn in Figure 10a: (1) the West Spitsbergen Current (WSC in red), (2) the Yermak Pass Branch (YPB in blue), (3) the Svalbard Branch (SB in green), and (4) the Yermak Branch (YB in magenta; Figure 11 and Table 2). We chose this temperature criterion as the Yermak Branch is mainly composed of water colder than 2°C at the beginning of the time series. The WSC shows large (the largest among the four sections) annual variations (Table 2) in agreement with those in Beszczynska-Möller et al. (2012; Figure 11a). The AW volume transport in the YPB (in blue) is largely correlated ($r = 0.65$) with the AW transport in the WSC (in red) and the YPB carries 31% (36% in winter) of the AW inflow from the WSC (Figure 11a). The volume transport of the YPB is sometime negative in summer, indicating a northwestward flow, as observed in the ADCP current data (Figure 8b). The model outputs suggest that the main pathway of the AW in winter over the Yermak Plateau is the YPB. The small SB transport (in green, mean of 0.4 Sv) is significantly correlated with the WSC transport ($r = 0.45$; Figure 11a). In summer, the volume transport is larger in the SB than in the YPB, in agreement with observations (e.g., Sirevaag & Fer, 2009). The YB volume transport is very small (mean 0.04 Sv), carries quite cold waters (between 1.5 and 2°C) and does not show any significant seasonal variations. The sum of the volume transport from the YPB, the SB, and the YB, the three branches that bring warm water from the WSC in the Arctic Ocean is largely correlated with the WSC volume transport ($r = 0.75$) and represents 46% of the volume transport of the WSC. Hence, in the model more than 50% of the WSC volume transport does not enter the Arctic Ocean and directly turns back with the Fram Strait recirculating branches, in agreement with Manley (1995) and Hattermann et al. (2016).

The model outputs suggest that the period sampled by the 2007–2008 mooring corresponded to a weak summer and an average winter YPB volume transport compared to volume transport values in the period 2007–2016 (Figure 11b, 1.1 Sv in winter 2007–2008 compared to 1.3 Sv on average over 2007–2017 and 0.13 Sv in summer 2008 compared to 0.6 Sv on average over 2007–2017). During some winters as winter 2011–2012, volume transport of AW through the Yermak Pass is twice as large as in 2008. The model suggests that the importance of the Yermak Pass Branch as a pathway of AW is modulated from one year to the other.

5. Summary and Discussion

We analyzed 14 months (July 2007 to September 2008) of ADCP data in the Yermak Pass at 80.601°N, 7.119°E on the 745 m isobath, a location covered by sea ice 10 months out of 12. The data set documents the unique intense high frequency velocity variations (80% of the total variance at periods less than 2 days) that mask a significant eddy activity and a large seasonal variation. We focused on the low-frequency variations and used 10 years of outputs from the Mercator-Ocean global ocean operational model to put the observations into a longer perspective. The model does not represent tides and does not explicitly resolve the Rossby radius in the area with its 1/12° grid. Yet we showed (section 4.1) that the model has skills in representing the AW inflow west and north of Svalbard. The three major results can be summarized as follows: (1) barotropic tides dominate the velocity signal in the Yermak Pass, (2) the winter AW flow composed of eddies and pulses is superimposed to tides, and (3) model outputs suggest that YPB carries 31% of the AW inflow from the WSC to the Arctic Ocean (36% in autumn/winter). The results are discussed below.

1. Ocean velocities in the Yermak Pass are dominated by high frequencies with strong diurnal and semidiurnal tide signals as observed in other locations of the Yermak Plateau (D'Asaro & Morison, 1992; Hunkins, 1986). Barotropic tides, well predicted in the AOTIM5 model, represent 73% and 97% of the northward and eastward variance respectively. It has been shown that the strong tidal currents over the Yermak Plateau lead to increased internal wave activity and turbulent mixing (Fer et al., 2010, 2015;

Padman & Dillon, 1991; Padman et al., 1992; Plueddemann, 1992, Wijesekera et al., 1993). The diapycnal mixing is large enough over the Yermak Plateau to influence the heat content of the Atlantic Water inflow entering in the Arctic and varies locally depending on topography and hydrography (Fer et al., 2015). Ocean to ice heat fluxes over the Yermak Plateau are large enough to melt the sea ice in summer (e.g., Fer et al., 2010; Meyer et al., 2017b; Peterson et al., 2017). They are expected to be even larger in late autumn/winter when the AW inflow is intense and warm and storms frequent and strong (e.g., Koenig et al., 2016; Provost et al., 2017; Rainville & Woodgate, 2009). As the profiler did not work, we lack temperature data to examine internal waves and diapycnal mixing. The tidal signal is essentially the only current component in summer and leads to a residual current of 4.3 cm/s to the northwest along bathymetry at 300 m in the AW core. In winter the mean current is small (2.6 cm/s) and orientated to the northeast perpendicular to isobaths, suggesting that other processes induce a mean current of 4.7 cm/s to the southeast in the AW core to counterbalance the residual tidal current.

2. Once tidal variability is removed, mesoscale activity with a baroclinic component dominates the flow through the Yermak Pass in winter. The largest energy peaks were found in the core of the AW (300 m) at period between 5 and 14 days (Figure 7). The time scales are consistent with the eddies that ARCTEMIZ88 drifting floats documented in the Yermak Pass at 300 m in the fall 1988 (Figure 1b; Gascard et al., 1995; Richez, 1998). Eddies are a dominant feature of the AW inflow in the Arctic (e.g., Padman & Dillon, 1991; Våge et al., 2016; Zhao et al., 2014). In the core of the AW, another conspicuous energy band is found at the monthly and bimonthly period (Figure 9). This is interpreted as episodes of intense AW. These pulses, occurring mainly in autumn-winter, correspond to a strong eastward flow carrying AW across the Yermak Plateau (Figure 8). The four ARCTEMIZ88 floats that made a U turn at 80.7°N and proceeded through the Yermak Pass were probably taken in an AW pulse and documented similar velocities. The ADCP data suggest that the pulses are accompanied with a shallowing of the pycnocline potentially allowing heat from the AW to reach the sea ice (Figure 3). The monthly scale variations in the WSC volume transport are determined by short-term variations in the offshore part of the WSC and of the westward recirculations at 78.5°N and 79°N (Beszczynska-Möller et al., 2012). Similarly, the monthly pulses in the YPB could be attributed to variations in the westward recirculating branch at 80.5°N (Figures 10a and 10b).
3. After evaluation, Mercator-Ocean operational model outputs were used to tentatively examine the evolution and the partition of the AW inflow downstream of the WSC. The model outputs confirm that the flow of the Atlantic Water through the Yermak Pass is a winter pattern associated with an overflow of the strong winter WSC. On average over 10 years, the volume transport of the Yermak Pass Branch (0.9 Sv $\pm$ 0.8) is equal to 31% of the volume transport of the West Spitsbergen Current (3.0 Sv $\pm$ 1.3) and, in winter, YPB is the main entrance of the Atlantic Water from Fram Strait to the Arctic Ocean. In agreement with Hattermann et al. (2016), the model outputs indicate that more than 50% of the AW inflow in the WSC recirculates back in Fram Strait and does not enter the Arctic Ocean. The Svalbard Branch (0.4 Sv $\pm$ 0.3) has a smaller volume transport than the Yermak Pass Branch in general and less seasonality. In the model, the Yermak Branch (0.04 Sv $\pm$ 0.2) is negligible. However, those numbers have to be considered with caution. Indeed Mercator-Ocean operational model does not simulate tides and does not take tides into account at all. Tides are a major player above and on the slopes of the Yermak Plateau and undoubtedly contribute to significantly altering the above figures. Indeed, Padman et al. (1992) argued that tidal rectification is probably responsible for the mean current of the YB. This could explain why the AW flow through the YB is so small in the model outputs. Luneva et al. (2015) compared two 30 year simulations of a 1/4° sea-ice ocean coupled model, one with explicitly resolved tides and the other without any tidal dynamics. They showed the important role of tides on the water mass mixing and sea ice in the Arctic Ocean. To properly resolve AW pathways and transport distribution north of Svalbard, an eddy-resolving model (1/36°) with explicitly simulated tides is needed.

Acknowledgments
The mooring work was supported by the European project Damocles and by funding from the ICE-ARC program from the European Union 7th Framework. The efforts of the captain and crew on board the R/V Haakon Mosby for the deployment and K/V Svalbard for the recovery are appreciated. Z. Koenig acknowledges a PhD scholarship from Université Pierre et Marie Curie (UPMC). The Mercator-Ocean global operational system is part of the Copernicus Marine Environment Monitoring Service (CMEMS; http://marine.copernicus.eu/) and data are available online (http://bulletin.mercator-ocean.fr/en/PSY4#2/75.5/-51.3). The ADCP mooring data in the Yermak Pass are publicly available in the SEANOE database: https://doi.org/10.17882/51023.

References

Beszczynska-Möller, A., Fahrbach, E., Schauer, U., & Hansen, E. (2012). Variability in Atlantic Water temperature and transport at the entrance to the Arctic Ocean, 1997–2010. *ICES Journal of Marine Science*, *69*, 852–863. https://doi.org/10.1093/icesjms/fss056

Beszczynska-Möller, A., von Appen, W.-J., & Fahrbach, E. (2015). Physical oceanography and current meter data from moorings F1–F14 and F15/F16 in the Fram Strait, 1997–2012. *PANGAEA*. https://doi.org/10.1594/PANGAEA.150016

Cokelet, E. D., Tervalon, N., & Bellingham, J. G. (2008). Hydrography of the West Spitsbergen Current, Svalbard Branch: Autumn 2001. *Journal of Geophysical Research*, *113*, C01006. https://doi.org/10.1029/2007JC004150

D'Asaro, E. A., & Morison, J. H. (1992). Internal waves and mixing in the Arctic Ocean. *Deep Sea Research, Part A: Oceanographic Research Papers*, *39*(Suppl. 2), S459–S484.

Dee, D. P., Uppala, S. M., Simmons, A. J., Berrisford, P., Poli, P., Kobayashi, S., . . . Vitart, F. (2011). The ERA-Interim reanalysis: Configuration and performance of the data assimilation system. *Quarterly Journal of the Royal Meteorological Society*, *137*, 553–597. https://doi.org/10.1002/qj.828

Ezraty, R., Girard-Ardhuin, F., Piolle, J., Kaleschke, F. L., & Heygster, G. (2007). *Arctic and Antarctic sea ice concentration and Arctic sea ice drift estimated from Special Sensor Microwave data, User's manual version 2.1*. Brest, France: CERSAT.

Fer, I., Müller, M., & Peterson, A. K. (2015). Tidal forcing, energetics, and mixing near the Yermak Plateau. *Ocean Science Discussions*, *11*(5), 287–304. https://doi.org/10.5194/os-11-287-2015

Fer, I., Skogseth, R., & Geyer, F. (2010). Internal waves and mixing in the Marginal Ice Zone near the Yermak Plateau. *Journal of Physical Oceanography*, *40*, 1613–1630. https://doi.org/10.1175/2010JPO4371.1

Gascard, J.-C., Beauverger, M., Lanousellé, J., Goff, H. L., Koenig, Z., & Provost, C. (2017). ADCP mooring data in 2007–2008 north of Svalbard over the Yermak Plateau in the Yermak Pass. *SEANOE*. https://doi.org/10.17882/51023

Gascard, J.-C., Richez, C., & Rouault, C. (1995). New insights on large-scale oceanography in Fram Strait: The West Spitsbergen Current. In W.O. Smith, Jr., & J. M. Greibmeier (Eds.), *Arctic oceanography, marginal ice zones and continental shelves* (Vol. 49, pp. 131–182). Washington, DC: American Geophysical Union.

Hattermann, T., Isachsen, P. E., von Appen, W.-J., Albretsen, J., & Sundfjord, A. (2016). Eddy-driven recirculation of Atlantic Water in Fram Strait. *Geophysical Research Letters*, *43*, 3406–3414. https://doi.org/10.1002/2016GL068323

Hunkins, K. (1986). Anomalous diurnal tidal currents on the Yermak Plateau. *Journal of Marine Research*, *44*(1), 51–69. https://doi.org/10.1357/002224086788460139

Ivanov, V. V., Polyakov, I., Dmitrenko, I., Hansen, E., Repina, I., Kirillov, S., . . . Timokov, L. (2009). Seasonal variability in the Atlantic Water off Spitsbergen. *Deep Sea Research, Part I: Oceanographic Research Papers*, *56*, 1–14. https://doi.org/10.1016/j.dsr.2008.07.013

Kawasaki, T., & Hasumi, H. (2016). The inflow of Atlantic Water at the Fram Strait and its interannual variability. *Journal of Geophysical Research: Oceans*, *121*, 502–519. https://doi.org/10.1002/2015JC011375

Koenig, Z., Provost, C., Villacieros-Robineau, N., Sennéchael, N., & Meyer, A. (2016). Winter ocean-ice interactions under thin sea ice observed by IAOOS platforms during N-ICE2015: Salty surface mixed layer and active basal melt. *Journal of Geophysical Research: Oceans*, *121*, 7898–7916. https://doi.org/10.1002/2016JC012195

Koenig, Z., Provost, C., Villacieros-Robineau, N., Sennéchael, N., Meyer, A., Lellouche, J.-M., & Garric, G. (2017). Atlantic Waters inflow north of Svalbard: Insights from IAOOS observations and Mercator Ocean global operational system during N-ICE2015. *Journal of Geophysical Research: Oceans*, *122*, 1254–1273. https://doi.org/10.1002/2016JC012424

Kowalik, Z., & Luick, J. (2013). *The oceanography of tides*. Retrieved from https://www.uaf.edu/files/sfos/Kowalik/tide_book.pdf

Lellouche, J. M., Le Galloudec, O., Drévillon, M., Régnier, C., Greiner, E., Garric, G., . . . de Nicola, C. (2012). Evaluation of real time and future global monitoring and forecasting systems at Mercator Océan. *Ocean Science Discussions*, *9*, 1123–1185.

Luneva, M. V., Aksenov, Y., Harle, J. D., & Holt, J. T. (2015). The effect of tides on the water mass mixing and sea ice in the Arctic Ocean. *Journal of Geophysical Research: Oceans*, *120*, 6669–6699. https://doi.org/10.1002/2014JC010310

Madec, G., & NEMO Team. (2008). *NEMO ocean engine. Note du Pole de modélisation* (Vol. 27). Versailles, France: Institute Pierre Simon Laplace.

Manley, T. O. (1995). Branching of Atlantic Water within the Greenland-Spitsbergen passage: An estimate of recirculation. *Journal of Geophysical Research*, *100*(C10), 20627–20634.

Manley, T. O., Bourke, R. H., & Hunkins, K. L. (1992). Near-surface circulation over the Yermak Plateau in northern Fram Strait. *Journal of Marine Systems*, *3*(1), 107–125.

Meyer, A., Fer, I., Sundfjord, A., & Peterson, A. K. (2017b). Mixing rates and vertical heat fluxes north of Svalbard from Arctic winter to spring. *Journal of Geophysical Research: Oceans*, *122*, 4569–4586. https://doi.org/10.1002/2016JC012441

Meyer, A., Sundfjord, A., Fer, I., Provost, C., Robineau, N. V., Koenig, Z., . . . Kauko, H. M. (2017a). Winter to summer oceanographic observations in the Arctic Ocean north of Svalbard. *Journal of Geophysical Research: Oceans*, *122*, 6218–6237. https://doi.org/10.1002/2016JC012391

Muench, R. D., McPhee, M. G., Paulson, C. A., & Morison, J. H. (1992). Winter oceanographic conditions in the Fram Strait and Yermak Plateau region. *Journal of Geophysical Research*, *97*(C3), 3469–3483.

Nurser, A. J. G., & Bacon, S. (2013). Eddy length scales and the Rossby radius in the Arctic Ocean. *Ocean Science Discussions*, *10*(5), 1807–1831.

Padman, L., & Dillon, T. (1991). Turbulent mixing near the Yermak Plateau during the Coordinated Eastern Arctic Experiment. *Journal of Geophysical Research*, *96*(C3), 4769–4782. https://doi.org/10.1029/90JC02260

Padman, L., & Erofeeva, S. (2004). A barotropic inverse tidal model for the Arctic Ocean. *Geophysical Research Letters*, *31*, L02303. https://doi.org/10.1029/2003GL019003

Padman, L., Plueddemann, A. J., Muench, R. D., & Pinkel, R. (1992). Diurnal tides near the Yermak Plateau. *Journal of Geophysical Research*, *97*(C8), 12639–12652. https://doi.org/10.1029/92JC01097

Peterson, A. K., Fer, I., McPhee, M. G., & Randelhoff, A. (2017). Turbulent heat and momentum fluxes in the upper ocean under Arctic sea ice. *Journal of Geophysical Research: Oceans*, *122*, 1439–1456. https://doi.org/10.1002/2016JC012283

Pham, D. T., Verron, J., & Roubaud, M. C. (1998). A singular evaluative extended Kalman filter for data assimilation in oceanography. *Journal of Marine Systems*, *16*, 323–340.

Plueddemann, A. J. (1992). Internal wave observations from the Arctic environmental drifting buoy. *Journal of Geophysical Research*, *97*(C8), 12619–12638. https://doi.org/10.1029/92JC01098

Polton, J. A. (2015). Tidally induced mean flow over bathymetric features: A contemporary challenge for high-resolution wide-area models. *Geophysical & Astrophysical Fluid Dynamics*, *109*, 207–215. https://doi.org/10.1080/03091929.2014.952726

Provost, C., Sennéchael, N., Miguet, J., Itkin, P., Rösel, A., Koenig, Z., . . . Granskog, M. A. (2017). Observations of flooding and snow-ice formation in a thinner Arctic sea-ice regime during the N-ICE2015 campaign: Influence of basal ice melt and storms. *Journal of Geophysical Research: Oceans*, *122*, 7115–7134. https://doi.org/10.1002/2016JC012011

Rainville, L., & Woodgate, R. A. (2009). Observations of internal wave generation in the seasonally ice-free Arctic. *Geophysical Research Letters*, *36*, L23604. https://doi.org/10.1029/2009GL041291

Richez, C. (1998). The West Spitsbergen Current as seen by SOFAR floats during the ARCTEMIZ 88 Experiment: Statistics, differential kinematic properties, and potential vorticity balance. *Journal of Geophysical Research*, *103*(C8), 15539–15565. https://doi.org/10.1029/97JC02421

Rudels, B. (2012). Arctic Ocean circulation and variability–advection and external forcing encounter constraints and local processes. *Ocean Science*, *8*(2), 261–286. https://doi.org/10.5194/os-8-261-2012

Sirevaag, A., & Fer, I. (2009). Early spring oceanic heat fluxes and mixing observed from drift stations north of Svalbard. *Journal of Physical Oceanography*, *39*(12), 3049–3069. https://doi.org/10.1175/2009JPO4172.1

Sirevaag, A., Rosa, S. D. L., Fer, I., Nicolaus, M., Tjernström, M., & McPhee, M. G. (2011). Mixing, heat fluxes and heat content evolution of the Arctic Ocean mixed layer. *Ocean Science*, *7*(3), 335–349. https://doi.org/10.5194/os-7-335-2011

Teigen, S. H., Nilsen, F., & Gjevik, B. (2010). Barotropic instability in the West Spitsbergen Current. *Journal of Geophysical Research*, *115*, C07016. https://doi.org/10.1029/2009JC005996

Teigen, S. H., Nilsen, F., Skogseth, R., Gjevik, B., & Beszczynska-Möller, A. (2011). Baroclinic instability in the West Spitsbergen Current. *Journal of Geophysical Research*, *116*, C07012. https://doi.org/10.1029/2011JC006974

Våge, K., Pickart, R. S., Pavlov, V., Lin, P., Torres, D. J., Ingvaldsen, R., . . . Proshutinsky, A. (2016). The Atlantic Water boundary current in the Nansen Basin: Transport and mechanisms of lateral exchange. *Journal of Geophysical Research: Oceans*, *121*, 6946–6960. https://doi.org/10.1002/2016JC011715

Von Appen, W.-J., Schauer, U., Hattermann, T., & Beszczynska-Möller, A. (2016). Seasonal cycle of mesoscale instability of the West Spitsbergen Current. *Journal of Physical Oceanography*, *46*, 1231–1254. https://doi.org/10.1175/JPO-D-15-0184.1

Wijesekera, H. W., Dillon, T. M., & Padman, L. (1993). Some statistical and dynamical properties of turbulence in the oceanic pycnocline. *Journal of Geophysical Research*, *98*(C12), 22665–22679. https://doi.org/10.1029/93JC02352

Zhao, M., Timmermans, M.-L., Cole, S., Krishfield, R., Proshutinsky, A., & Toole, J. (2014). Characterizing the eddy field in the Arctic Ocean halocline. *Journal of Geophysical Research: Oceans*, *119*, 8800–8817. https://doi.org/10.1002/2014JC010488